

Three-Dimensional Radiotherapy Dose Prediction on Head and Neck Cancer Patients with a Hierarchically Densely Connected U-net Deep Learning Architecture

Dan Nguyen, Xun Jia, David Sher, Mu-Han Lin, Zohaib Iqbal, Hui Liu, Steve Jiang

Medical Artificial Intelligence and Automation Laboratory, Department of Radiation Oncology, University of Texas Southwestern Medical Center, Dallas, TX, 75390, USA

Email: Dan.Nguyen@UTSouthwestern.edu

ABSTRACT

The treatment planning process for patients with head and neck (H&N) cancer is regarded as one of the most complicated due to large target volume, multiple prescription dose levels, and many radiation-sensitive critical structures near the target. Treatment planning for this site requires a high level of human expertise and a tremendous amount of effort to produce personalized high quality plans, taking as long as a week, which deteriorates the chances of tumor control and patient survival. To solve this problem, we propose to investigate a deep learning-based dose prediction model, Hierarchically Densely Connected U-net, based on two highly popular network architectures: U-net and DenseNet. We find that this new architecture is able to accurately and efficiently predict the dose distribution, outperforming the other two models, the Standard U-net and DenseNet, in homogeneity, dose conformity, and dose coverage on the test data. On average, our proposed model is capable of predicting the OAR max dose within 6.3% and mean dose within 5.1% of the prescription dose on the test data. The other models, the Standard U-net and DenseNet, performed worse, having an OAR max dose prediction error of 8.2% and 9.3%, respectively, and mean dose prediction error of 6.4% and 6.8%, respectively. In addition, our proposed model used 12 times less trainable parameters than the Standard U-net, and predicted the patient dose 4 times faster than DenseNet.

I. INTRODUCTION

Patients with head and neck (H&N) cancer undergoing radiotherapy have typically been treated with intensity modulated radiation therapy (IMRT)¹⁻⁷ and volume modulated arc therapy (VMAT)⁸⁻¹⁵, which has significantly reduced toxicity¹⁶⁻¹⁸ and improved quality of life^{19,20}, as compared to more conventional methods such as 3D conformal radiotherapy. However, treatment planning for this site is regarded as one of the most complicated due to several aspects, including large planning target volume (PTV) size²¹, multiple prescription dose levels that are simultaneously integrated boosted^{22,23}, and many radiation-sensitive organs-at-risk (OAR) that are in close proximity to the PTV²⁴⁻²⁷. Consequently, treatment planning for this site requires a tremendous level of human expertise and effort to produce personalized high quality plans.

In the typical current treatment planning workflow, a treatment planner solves an inverse optimization problem²⁸, where they adjust a set of hyper-parameters and weightings to control the tradeoffs between clinical objectives. Since the physician preferred plan is largely unknown, the planner meticulously tunes these parameters in a trial-and-error fashion in an attempt to reach an appropriate solution. Many rounds of consultation between the planner and physician occur regarding the plan quality and tradeoffs are discussed. Ultimately, this trial-and-error process in parameter tuning results in hours for a plan to be generated²⁹⁻³¹, and the iterations of consultation between the physician and planner may extend the treatment planning time up to one week. For aggressive H&N tumors, where tumor volume can double in approximately 30 days, which account for 50% of patients³², an extended planning time can greatly decrease local tumor control and patient survival³³⁻³⁶.

In recent years, the field of artificial intelligence (AI) and deep learning has made amazing progress, particularly in the field of computer vision and decision making. In 2015, Ronneberger et al. proposed a deep learning architecture for semantic segmentation, known as U-net³⁷. This neural network architecture, a type of convolutional neural network (CNN)³⁸ that falls under the class fully convolutional networks (FCN)³⁹, was capable of incorporating both local and global features to make a pixel-wise prediction. These predictions are commonly done slice-by-slice in 2D. For dose prediction, this 2D-based prediction can inherently cause some errors, particularly in slices at the superior and inferior edges of the PTV, thus motivating us to move towards 3D volumetric deep learning models. However, when creating a 3D variant of U-net, the computational expense grows with the dimensionality. Tradeoffs have to be made with the 3D version, such as less filters per convolution or max pooling layers. Attempts to combat this for 3D architectures focused on modifying portions of the architecture to be more efficient at propagating information, such as having a ResNet flavor of including skip connections during each block^{40,41}. With the currently available GPU technologies and memory, the network's performance is sacrificed.

A publication in 2017 by Huang et al. proposed a Densely Connected Convolutional Neural Network, also known as DenseNet⁴². The publication proposed the novel idea of densely connecting its convolutional maps together to promote feature propagation and reuse,

reduce the vanishing gradient issue, and decrease the number of trainable parameters needed. While the term “densely connected” was historically used to describe fully connected neural network layers, this publication by Huang et al. had adopted this terminology to describe how his convolutional layers were connected. While requiring more memory to use, the authors showed that the DenseNet was capable of achieving a better performance while having far less parameters in the neural network. For example, they were able to have comparable accuracy with ResNet, which had 10 million parameters, using their DenseNet, which had 0.8M parameters. This indicates that DenseNet is far more efficient in feature calculation than existing network architectures. For its contribution to the AI community, the DenseNet publication was awarded for the CVPR 2017 best publication. However, it is recognized that DenseNet, while efficient in parameter usage, actually utilizes considerably more GPU RAM, rendering a 3D U-net with fully densely connected convolutional connections infeasible for today’s current GPU technologies.

Motivated by a 3D densely connected U-net, but requiring less memory usage, we developed a neural network architecture that combines the essence of these two influential neural network architectures into our proposed network while maintaining a respectable RAM usage, which we call Hierarchically Densely Connected U-net (HD U-net). The term “hierarchically” is used here to describe the different levels of resolution in the U-net between each max pooling or upsampling operation. The convolutional layers are densely connected along each hierarchy, but not between hierarchies of the U-net during the upsampling operation. In particular, we wish to utilize the global and local information capabilities of U-net and the more efficient feature propagation and reuse of DenseNet. DenseNet alone is not expected to perform well for this task as we conjecture that the accurate prediction of dose distribution requires both global and local information, which DenseNet does not provide as a pixel-to-pixel mapping network. In this study, we will assess the proposed deep learning architecture on its capability to volumetrically predict the dose distribution for patients with H&N cancer, and compare its performance against the two deep learning models from which it was inspired from: U-net and DenseNet. The HD U-net and the 3D variants of U-net and DenseNet can all fit on a 11GB 1080 Ti GPU for unbiased comparison.

II. METHODS

II.1. H&N Patient Data

We acquired a total of 120 H&N patients for this study. Table 1 summarizes some of the patient information. The H&N cancer sites included base of tongue, lateral border of tongue, tonsillar fossa, glottis, supraglottis, thyroid, thyroid gland, larynx, mouth, mandible, pharynx, oropharynx, nasopharynx, hypopharynx, pyriform sinus, tonsil, retromolar area, parotid gland, bone, laryngeal cartilage, sublingual gland, nasal cavity, vallecula, aryepiglottic fold, lingual tonsil, maxillary sinus, laryngeal cartilage, parts of face, and trachea. The specific ICD codes of the patients used this study included C01, C09.0, 161.0, 193, C79.89, C32.9, C06.9, C32.8, 161.9, C12, C73, C09.8, C06.2, C07, 145.6, 161.1, C11.3, C79.51, C77.0, C32.3, C08.1, D10.6, C02.3, C11.1, C09.9, C49.0, 160.0, C10.0, C13.1, 141.6, C31.0, 147.9, C10.8, 161.3, C11.2, 141.0, 149.0, 141.2, 160.2, 146.0, 172.3, 146.9, C33, C13.2, C02.1, C32.1, C76.0, C41.1, C02.8, and C06.89

	Min	Median	Mean	Max
Age (yr)	18	60	61.43	91
Number of targets	1	3	2.94	5
Prescription dose (Gy)	42.5	60	61.51	72
Total target volume (cc)	38.75	700.06	706.73	1997.38
Body volume (cc)	10602.68	14451.15	13229.69	37060.00

Table 1: Summary of patient information

For each patient, we obtained the structure contours and the clinically delivered VMAT dose, calculated on the Eclipse Treatment Planning System. The voxel resolution of both the contours and dose were set to 5 mm³. As input, each OAR was set as separate binary masks, where each voxel is assigned 1 if the voxel is assigned to the OAR and 0 otherwise, in their own channel. The patient CT was not included as input for this study. The PTVs were included as their own channel, but instead of a binary mask, the mask was set to have a value equal the prescribed radiation dose. Each patient had 1-5 PTVs, with prescription doses ranging from 42.5 Gy to 72 Gy. In total, the input data used 23 channels to represent the OARs, PTVs, and prescription doses. Because we wished to input the prescription dose for the PTV's in Gy and then output the resulting in dose distribution in Gy, we chose not to normalize the data. This means the prediction model will have to learn how to propagate the prescription information directly. The 22 OARs used in this study are the body, left and right brachial plexus, brain, brainstem, left and right cerebellum, left and right cochlea, constrictors, esophagus, larynx, mandible, left and right masseter, oral cavity, post arytenoid & cricoid space (PACS), left and right parotid, left and right submandibular gland (SMG), and spinal cord. In the case that the patient was missing one of the 22 OARs, the corresponding channel was set to 0 for the input.

II.2. Deep Learning Architectures

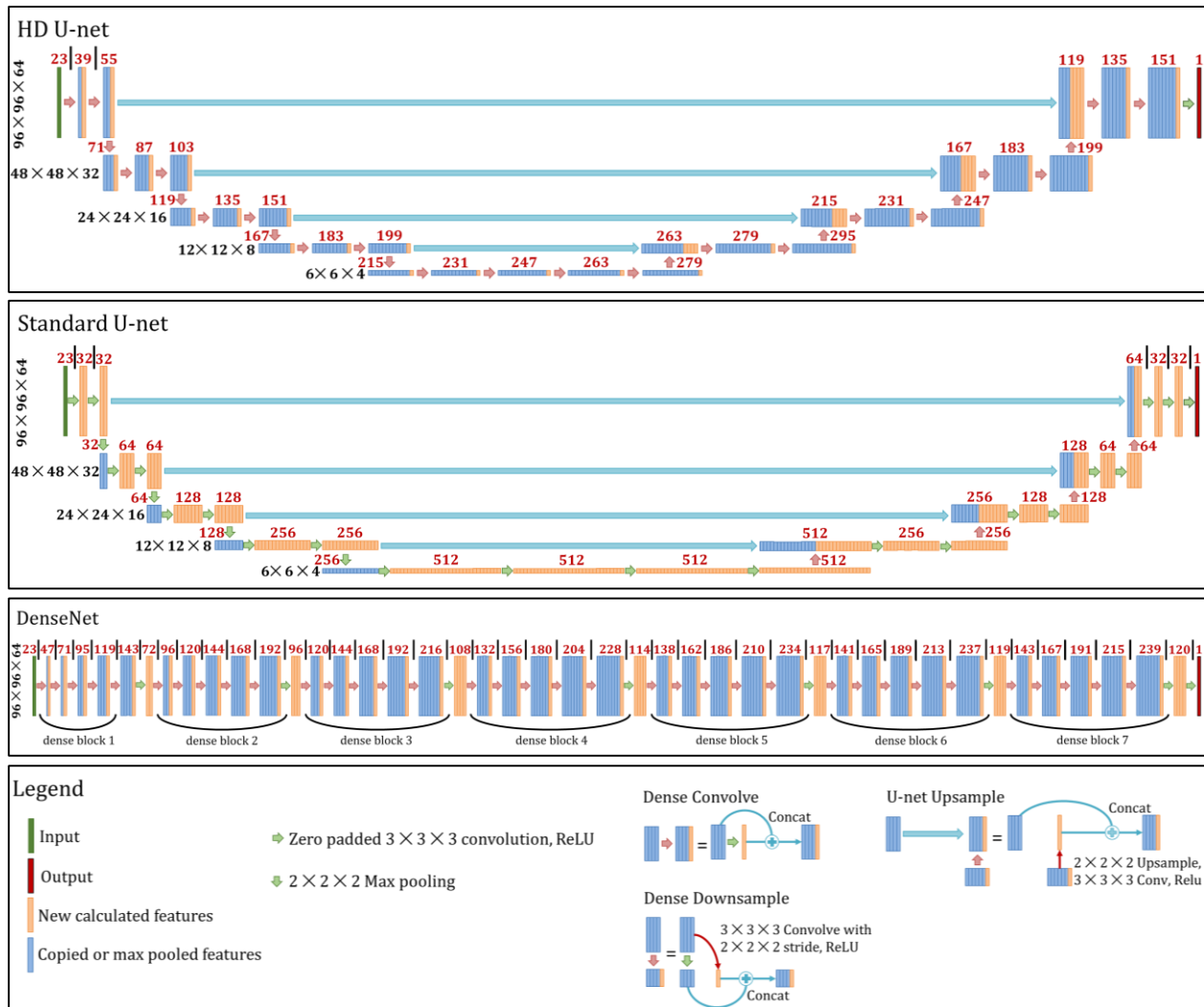


Figure 1: Architectures used within the study. Black numbers on the left side of the model represent the volume shape and resolution at a specific hierarchy. Red numbers represent the number of feature maps at a particular layer. Orange features represent the newly calculated features, and trainable parameters to learn, while blue features are copied or max pooled features that do not need trainable parameters.

Figure 1 shows all of the specific architectures that were used in the study. The HD U-net utilizes 3 operations defined in the legend: dense convolve, dense downsample and U-net upsample. The dense convolve effectively uses a standard convolution with ReLU, followed by a concatenation of the previous feature set. Performing this operation back-to-back is equivalent to the densely connected computation in the DenseNet publication. The dense downsampling operation is performed by a strided convolution and ReLU to calculate a new feature set that has half the resolution. The previous feature set is then max pooled and concatenated to the new feature set. Lastly, the U-net upsampling operation is done by up-sampling, convolution, and ReLU, followed by a concatenation of the feature set on the other side of the “U”. This “u-net upsampling” is the same operation used in the standard U-net,

with the upsample + convolve sometimes replaced with the transposed convolution. For each dense operation, a growth rate can be defined as the number new features calculated during the convolution step. Specifically, we utilized a growth rate of 16 (16 new features added after each “dense” operation), 4 dense downsampling operations, and 64 features returned during the upsampling operation.

To assess the performance of our implementation, our Hierarchically Dense (HD) U-net is compared to the two models which had inspired its design: the standard U-net and DenseNet. To fairly assess the architectures, the standard U-net, was constructed to match the HD U-net in terms of the number of downsampling operations used, and followed the conventional build of U-net, where the number of filters are doubled after each max pooling operation. It utilizes the regular convolution and max pooling, as defined in the green arrows in the legend in Figure 1.

DenseNet was constructed as outlined in the DenseNet publication, with dense-blocks followed by compression layers. Since DenseNet has an entirely different architecture than the U-nets, we simply chose to match the number of trainable parameters to HD U-net as close as possible. Ultimately, to meet this number of parameters, we chose to have 7 dense blocks, 5 dense convolutions per dense block, and a compression factor of 0.5. DenseNet utilizes the dense convolution during the dense block, and a normal convolution that reduces the number of layers by our set compression factor.

All networks were constructed to use 3D operations to handle the volumetric H&N data, and dropout was not used. L1 regularization, and L2 regularization were not used in the model. Batch normalization was briefly tested, but was ultimately removed in the final models, once it was determined that the exact prescription information, used as input, was more difficult to carry through the network with batch normalization. Exact details of each network is summarized in the appendix.

II.3. Training and Evaluation

Of the 120 H&N patients, we set aside 20 patients as testing data to evaluate at the end. To assess the performance and stability of each model—HD U-net, Standard U-net, and DenseNet—a 5-fold cross validation procedure was performed on the remaining 100 patients, where, for each fold, the patients were divided into 80 training patients and 20 validation patients. During each fold, the model would have its weights randomly initialized, and then update its weights based on the training set. The validation loss is used to determine the iteration that had the best model weights, a well-known method to help prevent from obtaining a model that has overfitted to the data^{43,44}. This instance of the model is then used to evaluate the validation data. After all models from every fold was trained, the models then evaluated the testing data.

Mean squared error between the predicted dose and the clinically delivered dose was used as the loss function for training each neural network model. The learning rate of each model

was adjusted to minimize the validation loss as a function of epochs. The patch size used for neural training was 96 x 96 x 64. Matching the U-net paper³⁷, we used a batch size of 1 sample. Instead of subdividing the patient contours and their corresponding dose volumes into set patches, each iteration of the model training process randomly selected a patch from the patient volume on-the-fly. Random patch selection also inherently adds stochastic translational shifts into the training data, which is one of the basic forms of data augmentation. While not the most robust data augmentation, this helps to somewhat reduce the overfitting issue, particularly for small datasets.

To equally compare across the patients, all plans were normalized such that the PTV with the highest corresponding prescription dose had 95% of its volume receiving 100% of the prescription dose (D_{95}). All dose statistics will also be reported relative to the prescription dose (i.e. the errors are reported as a percent of the prescription dose). As evaluation criteria PTV coverage (D_{98} , D_{99}), PTV max dose, homogeneity ($\frac{D_{2}-D_{98}}{D_{50}}$), van't Riet conformation number⁴⁵ ($\frac{(V_{PTV} \cap V_{100\%Iso})^2}{V_{PTV} \times V_{100\%Iso}}$), and the structure max and mean doses (D_{max} and D_{mean}) were evaluated.

To maintain consistency in performance, all neural network models were trained and evaluated on an NVIDIA GTX 1080 Ti GPU with 11 GB dedicated RAM.

III. RESULTS

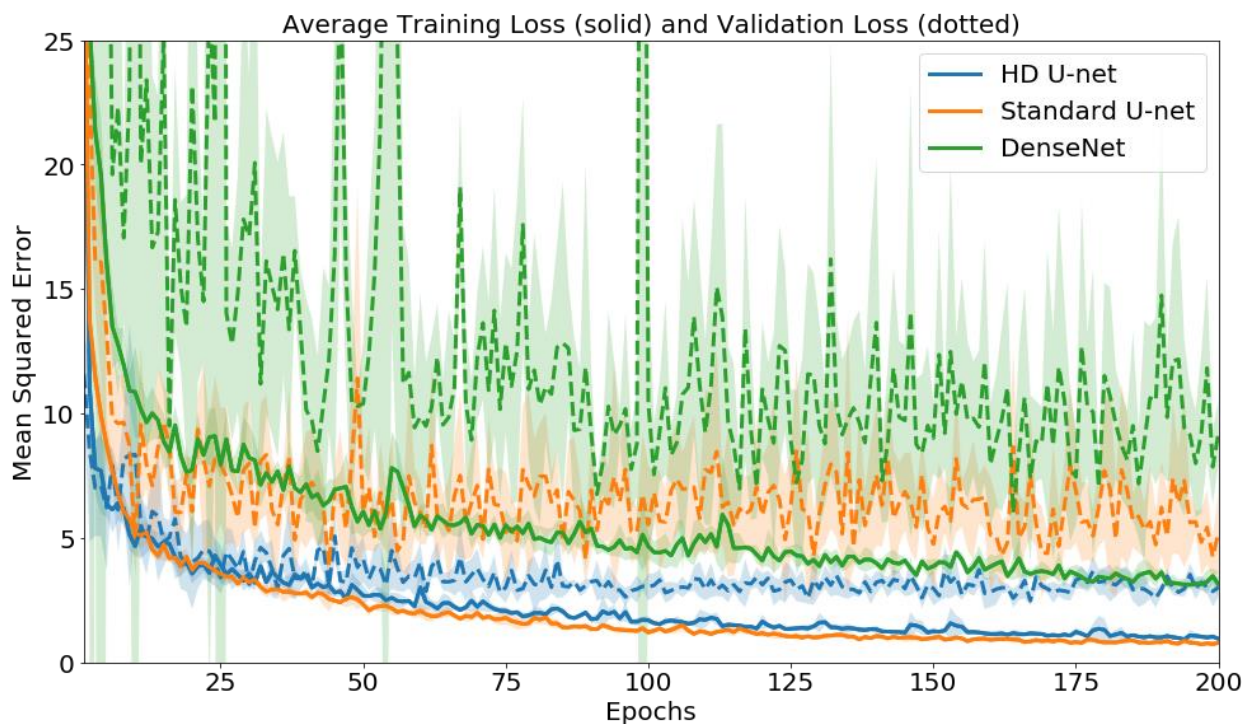


Figure 2: Mean loss across the 5 cross-validation folds for each model. The error equals 1 standard deviation.

Figure 2 shows the mean training and validation loss for the HD U-net, Standard U-net, and DenseNet. The HD and Standard U-net have a similar training loss as a function of epochs. However, the validation loss of the HD U-net is much lower and has less variation between the folds of the cross validation than that of the Standard U-net. This indicates that HD U-net is better at generalizing the modeling contours-to-dose, and is overfitting less to the training data. The DenseNet performed the worst for both the mean training and validation loss, as well as having the largest variation in the validation loss.

	Trainable parameters	Training Time (s) (averaged across cross validation folds) Mean \pm SD	Prediction time for entire patient volume (s) Mean \pm SD	
			Test	Cross-Val
HD U-net	3,289,006	11138.4 \pm 50.6	5.42 \pm 1.99	5.39 \pm 2.39
Standard U-net	40,068,385	8688.0 \pm 50.2	4.48 \pm 1.67	4.60 \pm 2.01
DenseNet	3,361,708	31764.0 \pm 53.7	17.12 \pm 6.42	18.05 \pm 7.97

Table 2: Trainable parameters and prediction time for each model.

Table 2 shows the number of trainable parameters and the prediction time for each model used in the study. The HD U-net and DenseNet have approximately 12 times less trainable parameters than the Standard U-net. The training time of HD U-net was about 3 hours, which is slightly longer than the Standard U-net’s time of 2.4 hours. DenseNet had the longest training time of 8.8 hours. The prediction time of the HD U-net is approximately 1 second longer for a full patient prediction, using patches of 96 x 96 x 64 and stride of 48 x 48 x 32. DenseNet had the longest prediction time of about 4 times longer than either of the U-nets.

PTV dose coverage and max dose									
Average values $\left(\frac{1}{n} \sum_{i=1}^n \frac{Value_i}{Prescription\ Dose_i}\right)$									
		D95		D98		D99		D _{max}	
		Mean ± SD	p-val	Mean ± SD	p-val	Mean ± SD	p-val	Mean ± SD	p-val
Test Results	Ground Truth	0.9999 ± 0.0002		0.99 ± 0.02		0.97 ± 0.03		1.04 ± 0.02	
	HD U-net	0.9999 ± 0.0005		0.99 ± 0.01		0.97 ± 0.02		1.07 ± 0.02	
	Standard U-net	1.0000 ± 0.0006		0.98 ± 0.02		0.96 ± 0.03		1.11 ± 0.03	
	DenseNet	0.9900 ± 0.0993		0.97 ± 0.10		0.96 ± 0.11		1.11 ± 0.16	
Cross-Validation Results	Ground Truth	1.0002 ± 0.0003		0.96 ± 0.07		0.91 ± 0.17		1.06 ± 0.04	
	HD U-net	1.0001 ± 0.0004		0.98 ± 0.03		0.94 ± 0.11		1.08 ± 0.03	
	Standard U-net	0.9999 ± 0.0005		0.98 ± 0.01		0.95 ± 0.14		1.13 ± 0.04	
	DenseNet	1.0001 ± 0.0004		0.98 ± 0.02		0.95 ± 0.11		1.09 ± 0.04	

Table 3: Average PTV coverage and max dose for the ground truth and the prediction models.

PTV dose coverage and max dose									
Average percent prediction error $\left(\frac{1}{n} \sum_{i=1}^n \frac{ Truth_i - Prediction_i }{Prescription\ Dose_i} \times 100\right)$									
		D95		D98		D99		D _{max}	
		Mean ± SD	p-val	Mean ± SD	p-val	Mean ± SD	p-val	Mean ± SD	p-val
Test Results	HD U-net	0.02 ± 0.05	0.621	1.18 ± 1.82	0.943	1.96 ± 2.14	0.918	3.75 ± 1.60	9.95 x 10 ⁻²⁸
	Standard U-net	0.03 ± 0.06	0.042	1.77 ± 2.35	0.017	2.65 ± 2.95	0.008	7.42 ± 3.26	4.51 x 10 ⁻³⁹
	DenseNet	1.01 ± 9.93	0.322	2.45 ± 10.13	0.008	3.42 ± 10.39	0.223	7.26 ± 15.37	7.95 x 10 ⁻⁰⁵
	HD U-net	0.02 ± 0.05	0.800	2.69 ± 6.13	0.096	6.02 ± 12.94	0.018	3.84 ± 3.13	1.23 x 10 ⁻⁵

Cross-Validation Results	Standard U-net	0.03 ± 0.06	0.446	2.86 ± 6.50	0.049	5.50 ± 9.69	0.007	7.64 ± 4.33	2.97 x 10 ⁻²⁵
	DenseNet	0.03 ± 0.06	0.315	2.82 ± 6.32	0.031	6.41 ± 13.59	0.004	5.02 ± 3.98	1.01 x 10 ⁻⁸

Table 4: PTV coverage and max dose prediction errors for each model.

Homogeneity and van't Riet conformation number			
Average values $\left(\frac{1}{n} \sum_{i=1}^n Value_i\right)$			
		Homogeneity $\left(\frac{D2-D98}{D50}\right)$	van't Riet conformation number
		Mean ± SD	Mean ± SD
Test Results	Ground Truth	0.06 ± 0.04	0.78 ± 0.06
	HD U-net	0.08 ± 0.02	0.76 ± 0.06
	Standard U-net	0.13 ± 0.04	0.74 ± 0.07
	DenseNet	0.12 ± 0.18	0.74 ± 0.12
Cross-Validation Results	Ground Truth	0.09 ± 0.09	0.74 ± 0.09
	HD U-net	0.10 ± 0.05	0.73 ± 0.08
	Standard U-net	0.14 ± 0.04	0.73 ± 0.08
	DenseNet	0.10 ± 0.04	0.74 ± 0.07

Table 5: Average homogeneity and van't Riet conformation numbers for the ground truth and the prediction models.

Homogeneity and van't Riet conformation number					
Average percent prediction error $\left(\frac{1}{n} \sum_{i=1}^n \frac{ Truth_i - Prediction_i }{1} \times 100\right)$					
		Homogeneity $\left(\frac{D2-D98}{D50}\right)$		van't Riet conformation number	
		Mean ± SD	p-val	Mean ± SD	p-val
Test Results	HD U-net	3.74 ± 1.78	4.05 x 10 ⁻¹⁴	3.08 ± 2.30	8.91 x 10 ⁻⁵
	Standard U-net	7.39 ± 3.99	2.54 x 10 ⁻²⁸	4.73 ± 4.30	3.40 x 10 ⁻¹³
	DenseNet	7.05 ± 17.39	7.95 x 10 ⁻⁵	6.28 ± 10.56	8.16 x 10 ⁻⁴
Cross-Validation Results	HD U-net	5.25 ± 6.76	0.292	4.84 ± 4.08	0.365
	Standard U-net	8.10 ± 6.04	3 x 10 ⁻⁷	6.12 ± 5.73	0.151

	DenseNet	6.11 ± 6.90	0.060	6.70 ± 5.21	0.970
--	----------	-----------------	-------	-----------------	-------

Table 6: Homogeneity and van't Riet conformation number prediction errors, taken as a percentage of the maximum of its achievable range. In our case, both homogeneity and the conformation number are defined to range from 0 to 1.

Table 3 shows the average values of the PTV coverage and max dose of the ground truth dose and the predicted clinical dose, and Table 4 shows the percent errors in the models' prediction on PTV coverage and max dose. While the models had similar performance in D98 and D99 for the cross-validation data, the HD U-net had better performance in predicting the dose coverage on the test set, indicating a more stable model for generalizing predictions outside of the validation and training sets used for manually tuning the hyperparameters and updating the model weights, respectively. This is also reflected in the p-values, where, for the test data, HD U-net differences against the ground truth were greater than 0.05, meaning the analysis could not find a statistically significant difference between HD U-net and Ground Truth, but did find statistically significant differences in the D98 and D99 for Standard U-net, and D98 for DenseNet. While, statistically, we the D_{\max} of the Ground Truth was significantly different than all 3 models' predictions, the HD U-net outperformed the other two networks in predicting the maximum dose to the PTV. Table 5 reports the average homogeneity indices and the van't Riet conformation numbers for the clinical dose and the predicted dose from the networks, and Table 6 shows the percent errors in the model's prediction of homogeneity and van't Riet conformation numbers. Statistically, the ground truth homogeneity and conformation were significantly different from the predictions for the test set. Aside from this, for the mean conformation number, the HD U-net performs similarly to the other models on the cross-validation data, and performs better on the test data than the other models. In terms of homogeneity, the HD U-net predicts similarly to ground truth compared to DenseNet, which are better both than that of the Standard U-net on the cross-validation data. On the test data, the HD U-net has better prediction performance on the homogeneity than the other two models.

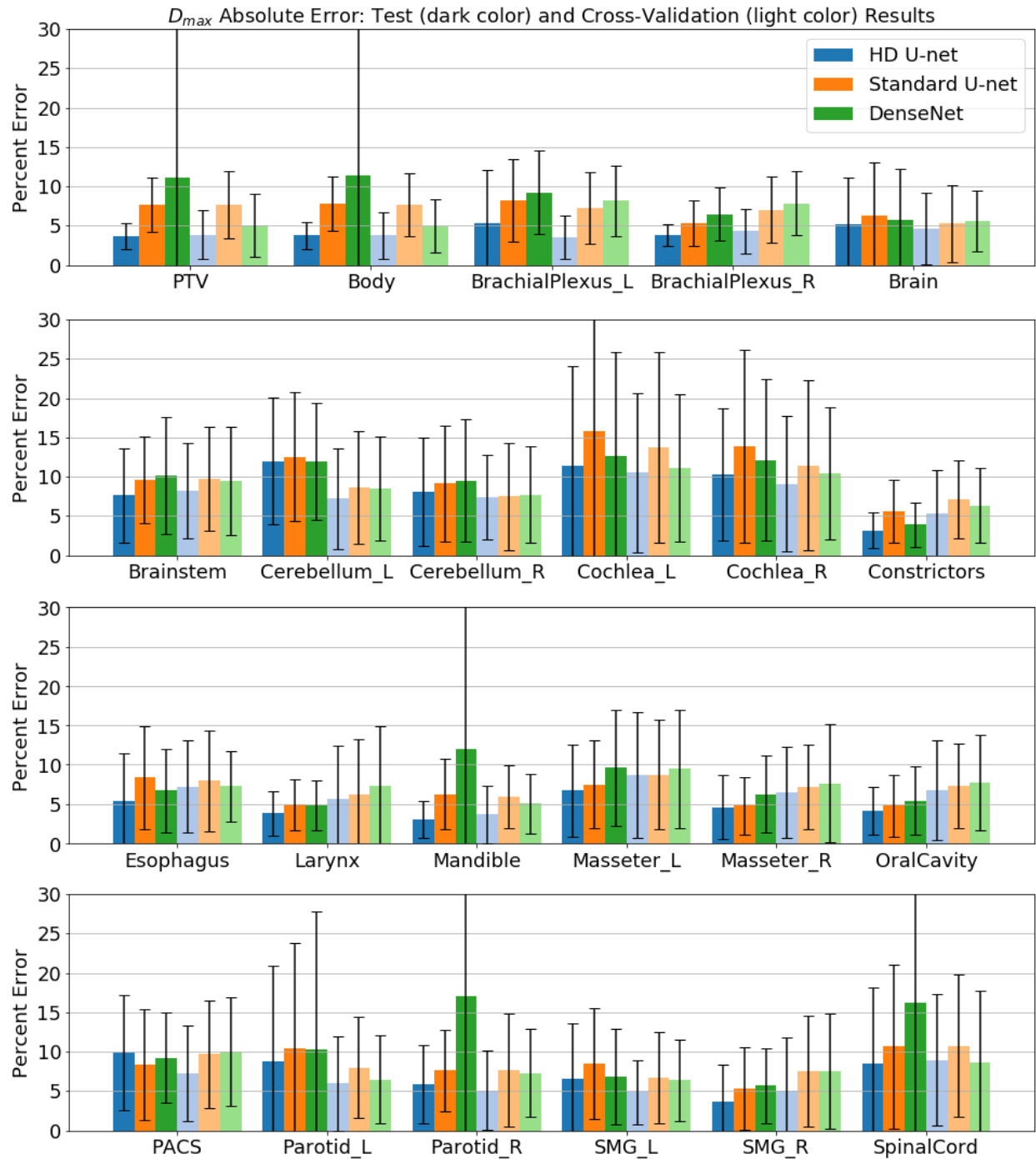


Figure 3: Absolute Error of D_{max} on the structures of interest. Error is reported as a percentage of the prescription dose.

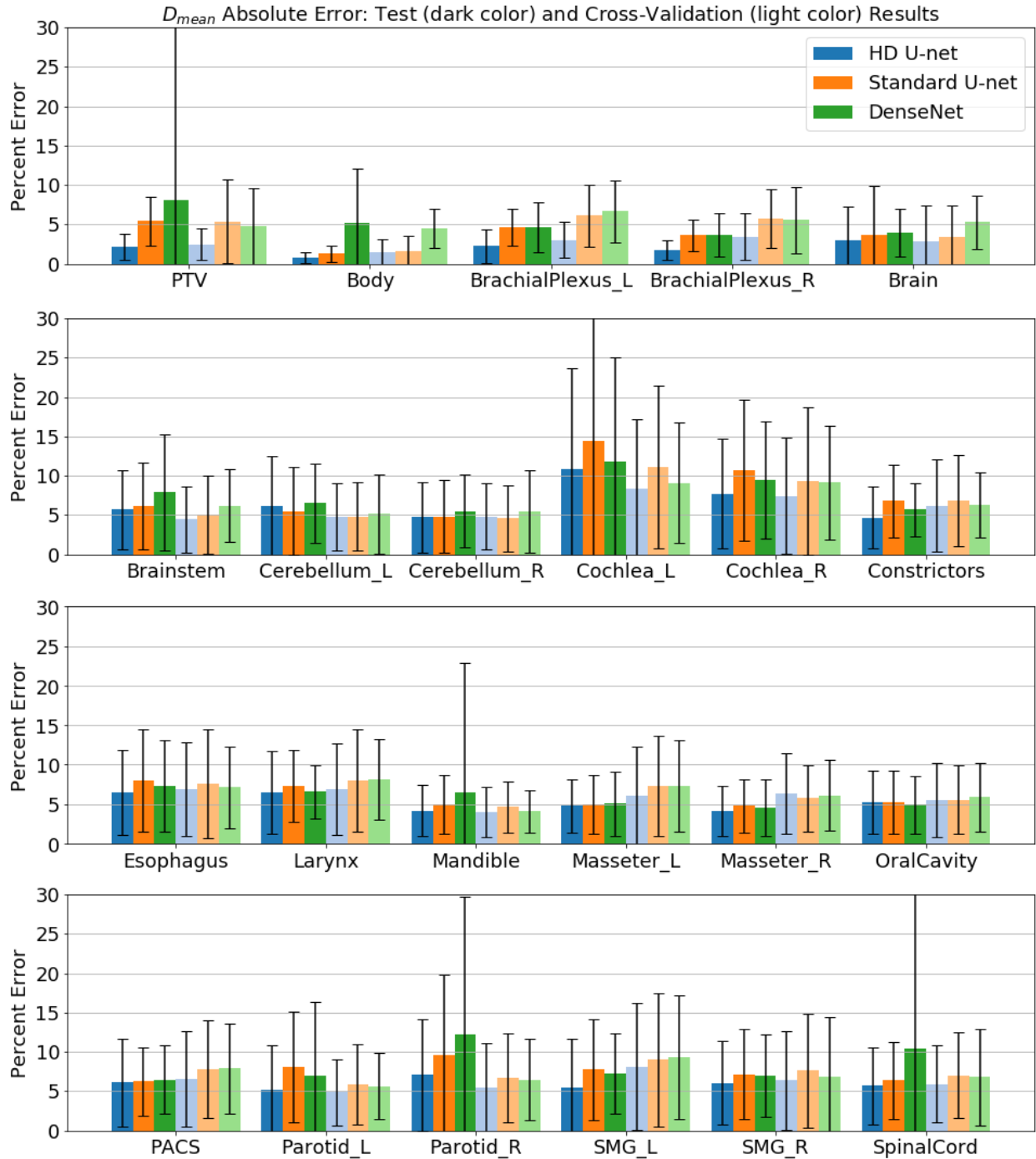


Figure 4: Absolute Error of D_{mean} on the structures of interest. Error is reported as a percentage of the prescription dose.

Figure 3 and Figure 4 show the D_{max} and D_{mean} absolute errors on all of the 22 structures and PTV. Due to the large variability in number of PTVs and prescription doses, percent errors are reported as a percent of the highest prescription dose for the patient, and the PTV D_{mean} and D_{max} calculation for Figure 3 and Figure 4 used the union of all the plan's PTVs as the region of interest. It can be easily seen that the HD U-net, shown in blue, has an overall lower

prediction error on the D_{\max} and D_{mean} than the other two networks in this study. For the cross-validation data, the HD U-net, Standard U-net, and DenseNet predicted, on average, the D_{\max} within $6.23 \pm 1.94\%$, $8.11 \pm 1.87\%$, and $7.65 \pm 1.67\%$, respectively, and the D_{mean} within $5.30 \pm 1.79\%$, $6.38 \pm 2.01\%$, and $6.49 \pm 1.43\%$, respectively, of the prescription dose. For the test data, the models predicted D_{\max} within $6.30 \pm 2.70\%$, $8.21 \pm 2.87\%$, and $9.30 \pm 3.44\%$, respectively, and D_{mean} within $5.05 \pm 2.13\%$, $6.40 \pm 2.63\%$, and $6.83 \pm 2.27\%$, respectively, of the prescription dose. Overall, the HD U-net had the best performance on both the cross-validation and test data. DenseNet had the largest discrepancy between its performance on the cross-validation data and test data, indicating its prediction volatility on data outside of its training and validation set.

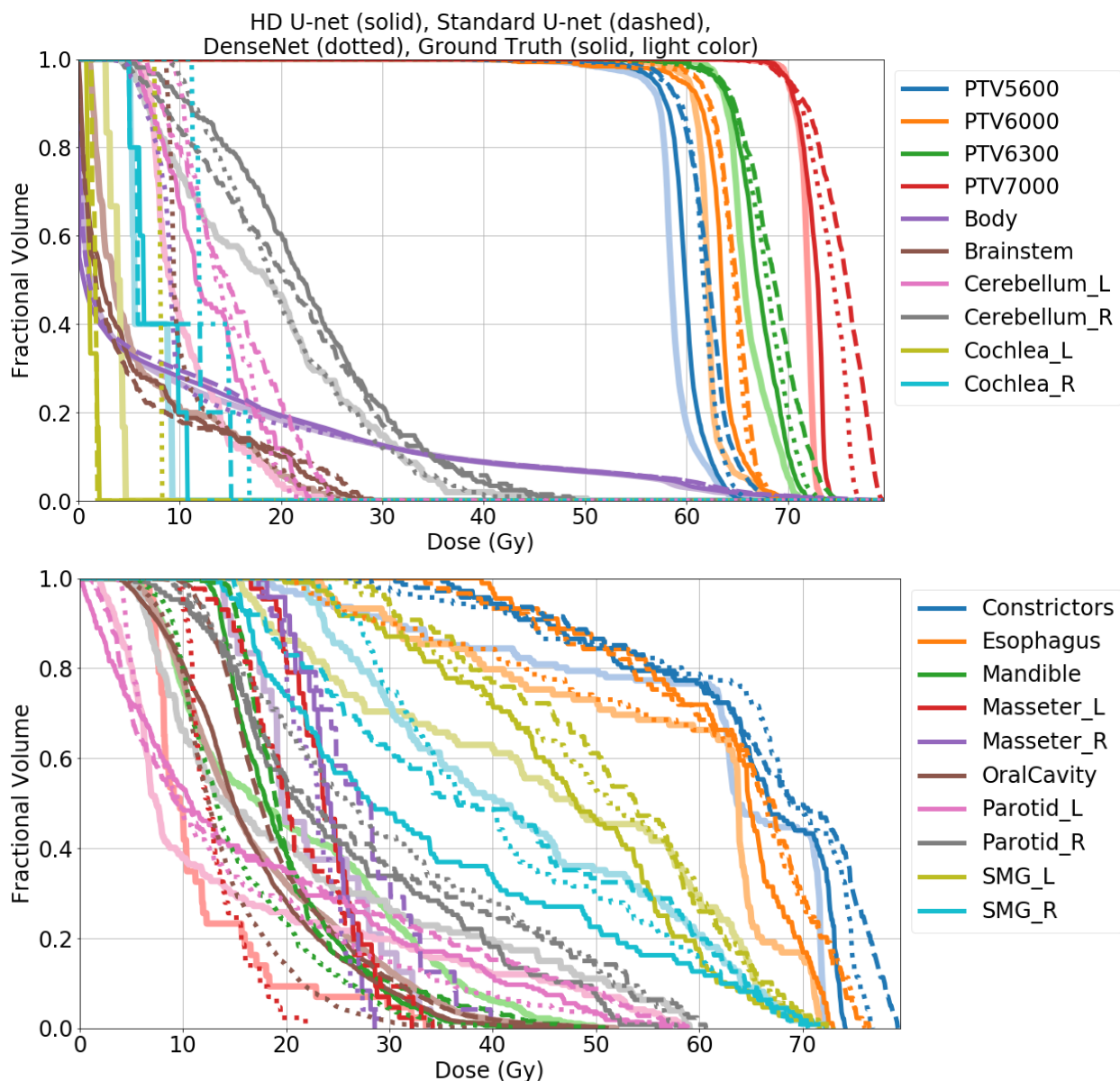


Figure 5: Dose volume histogram of an example patient from the test pool.

Figure 5 shows an example DVH from a patients from the test data. The solid line with the lighter color variant represents the clinical ground truth dose, while the darker color variants represent the predicted dose from HD U-net (solid), Standard U-net (dashed), and DenseNet (dotted). For this example patient, the HD U-net is superior to the other models in predicting the dose to the PTVs. Prediction of OAR dose are more variable between the models. This is also reflected in Figure 3 and Figure 4, where the standard deviation in prediction is small for the PTVs using the HD U-net, and larger on the OAR D_{\max} and D_{mean} prediction.

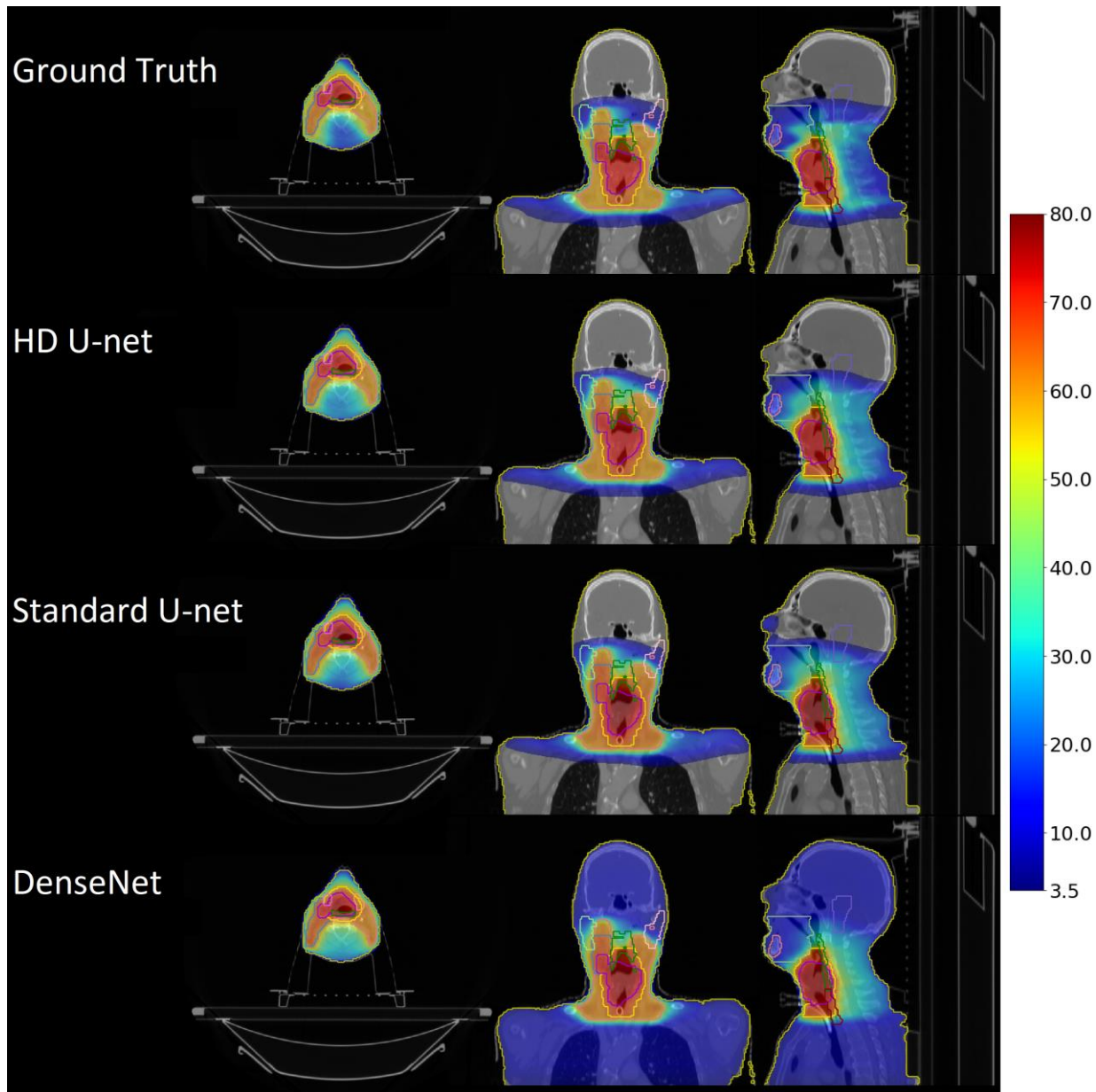


Figure 6: Dose washes of example patient from the test pool. Colorbar is shown in units of Gy. The clinical ground truth dose is shown on the top row, followed by the dose predictions of the HD U-net, Standard U-net, and DenseNet, respectively. Low dose cutoff for viewing was chosen to be 5% of the highest prescription dose (3.5 Gy).

Figure 6 shows the dose color wash for the same patient in Figure 5. Visually, the dose prediction models have comparable dose to the PTVs, with the Standard U-net and DenseNet slightly hotter than the HD U-net. The DenseNet also predicts dose above 3.5 Gy everywhere in the body, which is also reflected in the DVH in Figure 5 (purple dotted line) and the dose wash in Figure 6. The back of the neck is predicted to have more dose by all of the models, as compared to ground truth, which may represent a lack of data representation in the training data, or a lack of information being fed into the deep learning model itself.

IV. DISCUSSION

To our knowledge, this is the first instance of an accurate volumetric dose prediction for H&N cancer patients treated with VMAT. Existing plan prediction models are largely based around Knowledge Based Planning (KBP)⁴⁶⁻⁵⁹, with clinical/commercial implementations available known as Varian RapidPlan (Varian Medical Systems, Palo Alto, CA) and Pinnacle Auto-Planning Software (Philips Radiation Oncology Systems). These KBP methods have historically been designed to predict the DVH of a given patient, instead of the full volumetric dose prediction. The only exception is the study by Shiraishi and Moore⁵¹ in 2016, where they perform 3D dose prediction. However, their study is currently only evaluated on prostate patients, and thus the results are not comparable to our results for H&N patients. A study by Tol et al.⁶⁰ that evaluated RapidPlan on H&N cancer patients, had found that, in one of their evaluation groups, RapidPlan, had a mean prediction error of as large as 5.5 Gy on the submandibular gland, with the highest error on a single patient's OAR as high as 21.7 Gy on the lower larynx. Since their patients were clinically treated from 54.25 to 58.15 Gy, this translates to roughly 10% and 40% error, respectively in predictive performance. Another study by Krayenbuehl et al.⁶¹ had used Pinnacle Auto-Planning Software. However, in this study, the plan prediction aspect of the software was hidden from the user, and simply used as part of the auto-planning software itself, making this study's methodology not directly comparable to ours.

As a future study, we intend to perform a comprehensive evaluation and comparison of our dose prediction model against Varian RapidPlan. RapidPlan analyzes distance-to-target histograms—a relative geometrical relationship between an OAR and the PTV. In addition, RapidPlan incorporates relative overlap volume, relative out-of-field volume, absolute OAR volume, and absolute target volume⁶². Unlike our deep learning model, RapidPlan does not consider relationships between the OARs themselves, and thus does not account for tradeoffs between them. For an impartial comparison, both the RapidPlan and our dose prediction model must be trained and tested on the same data set. We plan to acquire a clean dataset that was used to train RapidPlan to accomplish an unbiased study.

It is currently a challenge to directly compare against other non-commercial prediction models, particularly since they are developed in-house and are proprietary to the institution that developed it. It is typically infeasible to obtain a copy or to faithfully replicate it to the exact specifications that were used by the originators. In addition, training and evaluation of

the model is usually performed using the institution's own data, and is often unavailable to the public to replicate the results or to train their own model for an unbiased comparison. These are common issues in the era of data driven modeling for the field of medicine, and while efforts to develop large public datasets exist, we have yet to reach the point where it is commonplace to use communal datasets for apples-to-apples comparisons.

Although the DenseNet had the poorest performance of the 3 models, it is due to the fact that the DenseNet is incapable of capturing global information into its prediction as the U-nets are capable of. This should not be seen as an oversight of DenseNet, as the authors of the paper proposed the concept of densely connected convolutional neural networks as a module, implying that this concept can be applied to more complex models. Their proposed DenseNet was used to illustrate the efficient feature propagation and reuse, alleviate the vanishing gradient, and reduce the number of parameters to moderate the overfitting issue. While DenseNet also had the slowest training and prediction time, it is possible that this issue may be alleviated with the newer GPUs, that are designed specifically for deep learning, such as the Volta architecture with tensor cores.

While accuracy tends to be positively correlated to a specific number of parameters in neural networks, the relationship is still not entirely clear between the accuracy and number of parameters, since neural networks are highly non-linear functions. Prediction time also tends to increase with more parameters and higher memory utilization, but is also affected by the breadth and depth of the network. Given the same number of trainable parameters, a fatter network with less layers will tend to predict more quickly than a skinny network with many layers, since the GPU can take advantage of the parallel computation.

The current main disadvantage of the densely connected architecture is that it requires a much larger memory usage, per trainable parameter, than standard networks. This is because it carries many of the past features it has calculated in memory in order to compute the next feature map. Xiaomeng et al. previously attempted to combat this with a hybrid densely connected U-net, where they combine a 2D Dense U-net, to extract intra-slice features, with a 3D counterpart for aggregating volumetric contexts⁶³. However, on a 12 GB RAM Titan Xp, the number of input slices they used at a time is 12, with feature maps containing only 3 slices during the dense block calculation. For radiotherapy, we require a much larger number of slices (e.g. 64) to make an accurate dose prediction, particularly for a complex site such as H&N. This makes the hybrid dense U-net by Xiaomeng et al. infeasible to use since it no longer fits on a modern GPU, hence our motivation for a less RAM intensive version of a densely connected U-net. Even with the extra memory cost, the expense is offset by the exceptionally efficient feature calculation. The Standard U-net, while capable of utilizing both the local and global information into its prediction still has considerable prediction error, indicating that either the model is not intelligent enough for the task, or it is not using its trainable parameters efficiently enough. In this study, we have shown, that by constructing a U-net with densely connected properties, we can take advantage of both U-net and DenseNet in our proposed model, and we are capable of reducing the total number

of trainable parameters by 12 fold while attaining a superior prediction result, as compared to the Standard U-net.

This dose prediction tool can currently be used as a clinical guidance tool, where the final tradeoff decisions and deliverable plan will still be made by the physician and dosimetrist. We plan to expand on this study and improve the model in several ways. First, to further reduce the prediction error to the OARs, we plan to incorporate the dose constraints, as prescribed by the physician, an input into the prediction model. Furthermore, we will examine the addition and effects of the CT image as input on the prediction accuracy. We expect that the addition of these types of information will prominently improve the deep learning model's performance, and will investigate to quantify their impact. In addition, we plan to develop and integrate a dose mimicking optimization⁶⁴ to convert our predicted dose into the best machine parameters to deliver the plan. As the field of artificial intelligence and deep learning continues to explosively progress, we will persistently investigate new deep learning concepts and architectures for more intelligent and efficient models to use. Eventually, our goal is to transition away from dose prediction based on historical plans to an AI-based treatment planning system, where we can push radiotherapy plans to improve and become better than that from current or past clinical practices.

V. CONCLUSION

We have developed and proposed a hierarchically densely connected U-net architecture, HD U-net, and applied the model to volumetric dose prediction for patients with H&N cancer. Using our proposed implementation, we are capable of accurately predicting the dose distribution from the PTV and OAR contours, and the prescription dose. On average, our proposed model is capable of predicting the OAR max dose within 6.3% and mean dose within 5.1% of the prescription dose on the test data. The other models, the Standard U-net and DenseNet, performed worse, having an OAR max dose prediction error of 8.2% and 9.3%, respectively, and mean dose prediction error of 6.4% and 6.8%, respectively. HD U-net also outperformed the other two models in homogeneity, dose conformity, and dose coverage on the test data. In addition, the proposed model is capable of using 12 times less trainable parameters than the Standard U-net, and predicted the patient dose 4 times faster than DenseNet. We plan to continue improving the model by incorporating more dose constraints and evaluating the addition of other data, such as the patient CT, on the model's predictive performance. Our long-term goal is the development of an artificially intelligence-based radiotherapy planning system.

VI. ACKNOWLEDGEMENTS

We would like to thank the support from Cancer Prevention and Research Institute of Texas (CPRIT) (IIRA RP150485, MIRA RP160661).

VII. REFERENCES

- 1 Brahme, A. Optimization of stationary and moving beam radiation therapy techniques. *Radiotherapy and Oncology* **12**, 129-140 (1988).
- 2 Bortfeld, T., Bürkelbach, J., Boesecke, R. & Schlegel, W. Methods of image reconstruction from projections applied to conformal radiotherapy. *Physics in Medicine and Biology* **35**, 1423 (1990).
- 3 Bortfeld, T. R., Kahler, D. L., Waldron, T. J. & Boyer, A. L. X-ray field compensation with multileaf collimators. *International Journal of Radiation Oncology* Biology* Physics* **28**, 723-730 (1994).
- 4 Webb, S. Optimisation of conformal radiotherapy dose distribution by simulated annealing. *Physics in Medicine and Biology* **34**, 1349 (1989).
- 5 Convery, D. & Rosenbloom, M. The generation of intensity-modulated fields for conformal radiotherapy by dynamic collimation. *Physics in Medicine and Biology* **37**, 1359 (1992).
- 6 Xia, P. & Verhey, L. J. Multileaf collimator leaf sequencing algorithm for intensity modulated beams with multiple static segments. *Medical Physics* **25**, 1424-1434, doi:<http://dx.doi.org/10.1118/1.598315> (1998).
- 7 Keller-Reichenbecher, M.-A. *et al.* Intensity modulation with the “step and shoot” technique using a commercial MLC: A planning study. *International Journal of Radiation Oncology* Biology* Physics* **45**, 1315-1324 (1999).
- 8 Yu, C. X. Intensity-modulated arc therapy with dynamic multileaf collimation: an alternative to tomotherapy. *Physics in Medicine and Biology* **40**, 1435 (1995).
- 9 Otto, K. Volumetric modulated arc therapy: IMRT in a single gantry arc. *Medical physics* **35**, 310-317 (2008).
- 10 Palma, D. *et al.* Volumetric Modulated Arc Therapy for Delivery of Prostate Radiotherapy: Comparison With Intensity-Modulated Radiotherapy and Three-Dimensional Conformal Radiotherapy. *International Journal of Radiation Oncology* Biology* Physics* **72**, 996-1001, doi:<http://dx.doi.org/10.1016/j.ijrobp.2008.02.047> (2008).
- 11 Shaffer, R. *et al.* Volumetric Modulated Arc Therapy and Conventional Intensity-modulated Radiotherapy for Simultaneous Maximal Intraprostatic Boost: a Planning Comparison Study. *Clinical Oncology* **21**, 401-407, doi:<http://dx.doi.org/10.1016/j.clon.2009.01.014> (2009).
- 12 Shaffer, R. *et al.* A Comparison of Volumetric Modulated Arc Therapy and Conventional Intensity-Modulated Radiotherapy for Frontal and Temporal High-Grade Gliomas. *International Journal of Radiation Oncology* Biology* Physics* **76**, 1177-1184, doi:<http://dx.doi.org/10.1016/j.ijrobp.2009.03.013> (2010).
- 13 Xing, S. M. C. a. X. W. a. C. T. a. M. W. a. L. Aperture modulated arc therapy. *Physics in Medicine & Biology* **48**, 1333 (2003).
- 14 Earl, M., Shepard, D., Naqvi, S., Li, X. & Yu, C. Inverse planning for intensity-modulated arc therapy using direct aperture optimization. *Physics in medicine and biology* **48**, 1075 (2003).
- 15 Daliang Cao and Muhammad, K. N. A. a. J. Y. a. F. C. a. D. M. S. A generalized inverse planning tool for volumetric-modulated arc therapy. *Physics in Medicine & Biology* **54**, 6725 (2009).

- 16 Marta, G. N. *et al.* Intensity-modulated radiation therapy for head and neck cancer: Systematic review and meta-analysis. *Radiotherapy and Oncology* **110**, 9-15, doi:<https://doi.org/10.1016/j.radonc.2013.11.010> (2014).
- 17 Toledano, I. *et al.* Intensity-modulated radiotherapy in head and neck cancer: Results of the prospective study GORTEC 2004–03. *Radiotherapy and Oncology* **103**, 57-62, doi:<https://doi.org/10.1016/j.radonc.2011.12.010> (2012).
- 18 Gupta, T. *et al.* Three-dimensional conformal radiotherapy (3D-CRT) versus intensity modulated radiation therapy (IMRT) in squamous cell carcinoma of the head and neck: A randomized controlled trial. *Radiotherapy and Oncology* **104**, 343-348, doi:<https://doi.org/10.1016/j.radonc.2012.07.001> (2012).
- 19 Rathod, S. *et al.* Quality-of-life (QOL) outcomes in patients with head and neck squamous cell carcinoma (HNSCC) treated with intensity-modulated radiation therapy (IMRT) compared to three-dimensional conformal radiotherapy (3D-CRT): Evidence from a prospective randomized study. *Oral Oncology* **49**, 634-642, doi:<https://doi.org/10.1016/j.oraloncology.2013.02.013> (2013).
- 20 Tribius, S. & Bergelt, C. Intensity-modulated radiotherapy versus conventional and 3D conformal radiotherapy in patients with head and neck cancer: Is there a worthwhile quality of life gain? *Cancer Treatment Reviews* **37**, 511-519, doi:<https://doi.org/10.1016/j.ctrv.2011.01.004> (2011).
- 21 Paulino, A. C., Koshy, M., Howell, R., Schuster, D. & Davis, L. W. Comparison of CT- and FDG-PET-defined gross tumor volume in intensity-modulated radiotherapy for head-and-neck cancer. *International Journal of Radiation Oncology*Biological*Physics* **61**, 1385-1392, doi:<https://doi.org/10.1016/j.ijrobp.2004.08.037> (2005).
- 22 Studer, G. *et al.* IMRT using simultaneously integrated boost (SIB) in head and neck cancer patients. *Radiation Oncology (London, England)* **1**, 7-7, doi:10.1186/1748-717X-1-7 (2006).
- 23 Wu, Q., Mohan, R., Morris, M., Lauve, A. & Schmidt-Ullrich, R. Simultaneous integrated boost intensity-modulated radiotherapy for locally advanced head-and-neck squamous cell carcinomas. I: dosimetric results. *International Journal of Radiation Oncology*Biological*Physics* **56**, 573-585, doi:[https://doi.org/10.1016/S0360-3016\(02\)04617-5](https://doi.org/10.1016/S0360-3016(02)04617-5) (2003).
- 24 Mayo, C., Yorke, E. & Merchant, T. E. Radiation Associated Brainstem Injury. *International Journal of Radiation Oncology • Biological • Physics* **76**, S36-S41, doi:10.1016/j.ijrobp.2009.08.078.
- 25 Kirkpatrick, J. P., van der Kogel, A. J. & Schultheiss, T. E. Radiation Dose–Volume Effects in the Spinal Cord. *International Journal of Radiation Oncology • Biological • Physics* **76**, S42-S49, doi:10.1016/j.ijrobp.2009.04.095.
- 26 Deasy, J. O. *et al.* Radiotherapy Dose–Volume Effects on Salivary Gland Function. *International Journal of Radiation Oncology • Biological • Physics* **76**, S58-S63, doi:10.1016/j.ijrobp.2009.06.090.
- 27 Rancati, T. *et al.* Radiation Dose–Volume Effects in the Larynx and Pharynx. *International Journal of Radiation Oncology • Biological • Physics* **76**, S64-S69, doi:10.1016/j.ijrobp.2009.03.079.
- 28 Oelfke, U. & Bortfeld, T. Inverse planning for photon and proton beams. *Medical dosimetry* **26**, 113-124, doi:10.1016/s0958-3947(01)00057-7 (2001).

- 29 Craft, D. L., Hong, T. S., Shih, H. A. & Bortfeld, T. R. Improved Planning Time and Plan Quality Through Multicriteria Optimization for Intensity-Modulated Radiotherapy. *International Journal of Radiation Oncology*Biophysics* **82**, e83-e90, doi:<https://doi.org/10.1016/j.ijrobp.2010.12.007> (2012).
- 30 Schreiner, L. J. On the quality assurance and verification of modern radiation therapy treatment. *Journal of medical physics/Association of Medical Physicists of India* **36**, 189 (2011).
- 31 Van Dye, J., Batista, J. & Bauman, G. S. Accuracy and uncertainty considerations in modern radiation oncology. *The Modern Technology of Radiation Oncology* **3**, 361-412 (2013).
- 32 Jensen, A. R., Nellesmann, H. M. & Overgaard, J. Tumor progression in waiting time for radiotherapy in head and neck cancer. *Radiotherapy and Oncology* **84**, 5-10, doi:<https://doi.org/10.1016/j.radonc.2007.04.001> (2007).
- 33 Bese, N. S., Hendry, J. & Jeremic, B. Effects of Prolongation of Overall Treatment Time Due To Unplanned Interruptions During Radiotherapy of Different Tumor Sites and Practical Methods for Compensation. *International Journal of Radiation Oncology • Biology • Physics* **68**, 654-661, doi:10.1016/j.ijrobp.2007.03.010.
- 34 González Ferreira, J. A., Jaén Olasolo, J., Azinovic, I. & Jeremic, B. Effect of radiotherapy delay in overall treatment time on local control and survival in head and neck cancer: Review of the literature. *Reports of Practical Oncology and Radiotherapy* **20**, 328-339, doi:10.1016/j.rpor.2015.05.010 (2015).
- 35 Fowler, J. F. & Lindstrom, M. J. Loss of local control with prolongation in radiotherapy. *International Journal of Radiation Oncology*Biophysics* **23**, 457-467, doi:[https://doi.org/10.1016/0360-3016\(92\)90768-D](https://doi.org/10.1016/0360-3016(92)90768-D) (1992).
- 36 Fein, D. A. *et al.* Do overall treatment time, field size, and treatment energy influence local control of T1-T2 squamous cell carcinomas of the glottic larynx? *International Journal of Radiation Oncology*Biophysics* **34**, 823-831, doi:[https://doi.org/10.1016/0360-3016\(95\)02205-8](https://doi.org/10.1016/0360-3016(95)02205-8) (1996).
- 37 Ronneberger, O., Fischer, P. & Brox, T. U-net: Convolutional networks for biomedical image segmentation. *International Conference on Medical Image Computing and Computer-Assisted Intervention*, 234-241 (2015).
- 38 LeCun, Y. *et al.* Backpropagation applied to handwritten zip code recognition. *Neural computation* **1**, 541-551 (1989).
- 39 Long, J., Shelhamer, E. & Darrell, T. Fully convolutional networks for semantic segmentation. *Proceedings of the IEEE Conference on Computer Vision and Pattern Recognition*, 3431-3440 (2015).
- 40 Milletari, F., Navab, N. & Ahmadi, S.-A. V-net: Fully convolutional neural networks for volumetric medical image segmentation. *3D Vision (3DV), 2016 Fourth International Conference on*, 565-571 (2016).
- 41 He, K., Zhang, X., Ren, S. & Sun, J. Deep residual learning for image recognition. *Proceedings of the IEEE conference on computer vision and pattern recognition*, 770-778 (2016).
- 42 Huang, G., Liu, Z., van der Maaten, L. & Weinberger, K. Q. Densely Connected Convolutional Networks. *Proc Cvpr Ieee* **1**, 2261-2269, doi:10.1109/Cvpr.2017.243 (2017).

- 43 Prechelt, L. Automatic early stopping using cross validation: quantifying the criteria. *Neural Networks* **11**, 761-767 (1998).
- 44 Caruana, R., Lawrence, S. & Giles, C. L. Overfitting in neural nets: Backpropagation, conjugate gradient, and early stopping. *Advances in neural information processing systems*, 402-408 (2001).
- 45 Van't Riet, A., Mak, A. C., Moerland, M. A., Elders, L. H. & van der Zee, W. A conformation number to quantify the degree of conformality in brachytherapy and external beam irradiation: application to the prostate. *International Journal of Radiation Oncology* Biology* Physics* **37**, 731-736 (1997).
- 46 Zhu, X. *et al.* A planning quality evaluation tool for prostate adaptive IMRT based on machine learning. *Medical physics* **38**, 719-726 (2011).
- 47 Appenzoller, L. M., Michalski, J. M., Thorstad, W. L., Mutic, S. & Moore, K. L. Predicting dose-volume histograms for organs-at-risk in IMRT planning. *Medical physics* **39**, 7446-7461 (2012).
- 48 Wu, B. *et al.* Improved robotic stereotactic body radiation therapy plan quality and planning efficacy for organ-confined prostate cancer utilizing overlap-volume histogram-driven planning methodology. *Radiotherapy and Oncology* **112**, 221-226 (2014).
- 49 Shiraishi, S., Tan, J., Olsen, L. A. & Moore, K. L. Knowledge-based prediction of plan quality metrics in intracranial stereotactic radiosurgery. *Medical physics* **42**, 908-917 (2015).
- 50 Moore, K. L., Brame, R. S., Low, D. A. & Mutic, S. Experience-Based Quality Control of Clinical Intensity-Modulated Radiotherapy Planning. *International Journal of Radiation Oncology* Biology* Physics* **81**, 545-551, doi:<https://doi.org/10.1016/j.ijrobp.2010.11.030> (2011).
- 51 Shiraishi, S. & Moore, K. L. Knowledge-based prediction of three-dimensional dose distributions for external beam radiotherapy. *Medical physics* **43**, 378-387 (2016).
- 52 Wu, B. *et al.* Patient geometry-driven information retrieval for IMRT treatment plan quality control. *Medical Physics* **36**, 5497-5505, doi:10.1118/1.3253464 (2009).
- 53 Wu, B. *et al.* Data-Driven Approach to Generating Achievable Dose-Volume Histogram Objectives in Intensity-Modulated Radiotherapy Planning. *International Journal of Radiation Oncology* Biology* Physics* **79**, 1241-1247, doi:<https://doi.org/10.1016/j.ijrobp.2010.05.026> (2011).
- 54 Wu, B. *et al.* Using overlap volume histogram and IMRT plan data to guide and automate VMAT planning: A head-and-neck case study. *Medical Physics* **40**, 021714-n/a, doi:10.1118/1.4788671 (2013).
- 55 Tran, A. *et al.* Predicting liver SBRT eligibility and plan quality for VMAT and 4π plans. *Radiation Oncology* **12**, 70, doi:10.1186/s13014-017-0806-z (2017).
- 56 Yuan, L. *et al.* Quantitative analysis of the factors which affect the interpatient organ-at-risk dose sparing variation in IMRT plans. *Medical Physics* **39**, 6868-6878, doi:10.1118/1.4757927 (2012).
- 57 Lian, J. *et al.* Modeling the dosimetry of organ-at-risk in head and neck IMRT planning: An intertechnique and interinstitutional study. *Medical Physics* **40**, 121704-n/a, doi:10.1118/1.4828788 (2013).
- 58 Folkerts, M. M., Gu, X., Lu, W., Radke, R. J. & Jiang, S. B. SU-G-TeP1-09: Modality-Specific Dose Gradient Modeling for Prostate IMRT Using Spherical Distance Maps of

- PTV and Isodose Contours. *Medical Physics* **43**, 3653-3654, doi:10.1118/1.4956999 (2016).
- 59 Folkerts, M. M. *et al.* Knowledge-Based Automatic Treatment Planning for Prostate IMRT Using 3-Dimensional Dose Prediction and Threshold-Based Optimization. *American Association of Physicists in Medicine* (2017).
- 60 Tol, J. P., Delaney, A. R., Dahele, M., Slotman, B. J. & Verbakel, W. F. Evaluation of a knowledge-based planning solution for head and neck cancer. *International Journal of Radiation Oncology• Biology• Physics* **91**, 612-620 (2015).
- 61 Krayenbuehl, J., Norton, I., Studer, G. & Guckenberger, M. Evaluation of an automated knowledge based treatment planning system for head and neck. *Radiation Oncology* **10**, 226 (2015).
- 62 Varian Medical Systems, I. RapidPlan Knowledge-Based Planning Frequently Asked Questions. (2018).
<https://www.varian.com/sites/default/files/resource_attachments/RapidPlanFAQs_RAD10321B.pdf>.
- 63 Li, X. *et al.* H-DenseUNet: Hybrid Densely Connected UNet for Liver and Tumor Segmentation from CT Volumes. *IEEE Transactions on Medical Imaging* (2018).
- 64 Long, T., Chen, M., Jiang, S. B. & Lu, W. Threshold-driven optimization for reference-based auto-planning. *Physics in medicine and biology* (2018).

APPENDIX

A.1. Details on deep learning architectures used in study

Layer number	HD U-net		Standard U-net		DenseNet	
	Layer type	Number features / channels	Layer type	Number features / channels	Layer type	Number features / channels
1	Input	23	Input	23	Input	23
2	Dense Conv	39	Conv	32	Dense Conv	47
3	Dense Conv	55	Conv	32	Dense Conv	71
4	Dense Downsample	71	Max Pooling	32	Dense Conv	95
5	Dense Conv	87	Conv	64	Dense Conv	119
6	Dense Conv	103	Conv	64	Dense Conv	143
7	Dense Downsample	119	Max Pooling	64	Conv	72
8	Dense Conv	135	Conv	128	Dense Conv	96
9	Dense Conv	151	Conv	128	Dense Conv	120
10	Dense Downsample	167	Max Pooling	128	Dense Conv	144
11	Dense Conv	183	Conv	256	Dense Conv	168
12	Dense Conv	199	Conv	256	Dense Conv	192
13	Dense Downsample	215	Max Pooling	256	Conv	96
14	Dense Conv	231	Conv	512	Dense Conv	120
15	Dense Conv	247	Conv	512	Dense Conv	144
16	Dense Conv	263	Conv	512	Dense Conv	168

17	Dense Conv	279	Conv	512	Dense Conv	192
18	U-net Upsample	263	U-net Upsample	512	Dense Conv	216
19	Dense Conv	279	Conv	256	Conv	108
20	Dense Conv	295	Conv	256	Dense Conv	132
21	U-net Upsample	215	U-net Upsample	256	Dense Conv	156
22	Dense Conv	231	Conv	128	Dense Conv	180
23	Dense Conv	247	Conv	128	Dense Conv	204
24	U-net Upsample	167	U-net Upsample	128	Dense Conv	228
25	Dense Conv	183	Conv	64	Conv	114
26	Dense Conv	199	Conv	64	Dense Conv	138
27	U-net Upsample	119	U-net Upsample	64	Dense Conv	162
28	Dense Conv	135	Conv	32	Dense Conv	186
29	Dense Conv	151	Conv	32	Dense Conv	210
30	Conv	1	Conv	1	Dense Conv	234
31					Conv	117
32					Dense Conv	141
33					Dense Conv	165
34					Dense Conv	189
35					Dense Conv	213
36					Dense Conv	237
37					Conv	119
38					Dense Conv	143
39					Dense Conv	167
40					Dense Conv	191
41					Dense Conv	215
42					Dense Conv	239
43					Conv	120
44					Conv	1

Table 7: Details of deep learning architectures. Dense Conv and U-net Upsample follow the notation outlined in Figure 1. All convolutions mentioned in this table use 3 x 3 x 3 kernels and are followed by the ReLU non-linear activation.